Journal of
Materials Chemistry A

ROYAL SOCIETY
OF CHEMISTRY

PAPER

View Article Online
View Journal | View Issue

Cite this: *J. Mater. Chem. A*, 2024, **12**, 31173

Point-defect chemistry for ionic conduction in solid electrolytes with isovalent cation mixing†

Takafumi Ogawa, *[a] Kazuyuki Sato,[b] Kazuhiro Mori,[c] Shunsuke Kobayashi,[a] Hiroki Moriwake,[a] Yuichi Ikuhara[ad] and Akihide Kuwabara[a]

Recent studies on solid electrolytes for electrochemical devices such as batteries and fuel cells have focused on investigating migration of mobile ions in ion-conducting crystalline solids, whereas the temperature dependence of the concentrations of charge carriers has received little attention. In this study, the role of point-defect concentrations on the conductivity of fluoride ions in BaF_2–CaF_2 solid solution was investigated using first-principles calculations. The BaF_2–CaF_2 solid solution exhibits ionic conductivity that is several orders of magnitude higher than that of the unmixed compounds, BaF_2 and CaF_2. The calculated equilibrium point-defect concentration of a mixed structure with a composition of $Ba_{0.5}Ca_{0.5}F_2$ and unmixed structures shows that the cation mixing enhances anion Frenkel-pair concentrations by several orders of magnitudes. Although doped ions have the same valence state as that of an ion of a host material, a size mismatch between the doped and host ions could increase mobile defects. Activation, migration, and formation energies of mobile fluorine defects are compared among the examined structures by employing molecular dynamics simulations combined with machine-learning potentials and nudged elastic band calculations. The defect formation energy in the mixed phase is at least 0.75 eV lower than that in the unmixed cases, whereas the difference in migration energy is less than 0.15 eV. These results indicate that the increase in defect concentrations caused by cation mixing contributes to the enhancement of ionic conductivity. The formation energies of fluoride-ion vacancies and interstitial fluoride ions were also compared among fluorite-structured AF_2 (A = Ca, Sr, Ba, Cd and Pb), which exhibits opposite trends between the two defects except for PbF_2 when plotting as a function of ionic radius. The observed trends of the vacancy and interstitial defects correlate with the bonding strength parameter between neighboring F and A atoms and the space size of the interstitial site, respectively. The exceptional behavior of PbF_2 is attributed to $6s^2$ lone-pair electrons of Pb^{2+}. In $Ba_{0.5}Ca_{0.5}F_2$, the formation energy of each defect is close to the lower energy between BaF_2 and CaF_2, resulting in enhanced defect concentrations. The results indicate that the complementary exploitation of point-defect chemistry can provide a comprehensive understanding of the ionic conduction mechanism, leading to the rational design of materials with higher ionic conductivity.

Received 14th August 2024
Accepted 16th October 2024

DOI: 10.1039/d4ta05684a

rsc.li/materials-a

1 Introduction

Solid-state ionic conductors for energy conversion, energy storage and sensing have continuously attracted attention because of increasing demands for more efficient and safe power utilization with lower environmental loads, whose applications include lithium-ion and other cation batteries,[1,2] proton and oxide-ion conducting solid oxide fuel cells[3,4] and fluoride-ion batteries.[5,6] Understanding the atomistic mechanism governing electrical conductivity in such solid electrolytes and achieving higher conductivity have been the focus of previous studies. Thus, considerable effort has been dedicated to elucidating the migration mechanism of mobile ions transferring charges,[7,8] which includes exploring collective (or correlated) dynamics between ions and vicinal ions or polyhedra, as well as rotational dynamics or effects of the connectivity of constituent polyhedra.[9–17] Theoretical studies of ionic conduction mechanisms assume that the concentration of mobile species is independent of temperature. Thus, in this study, the validity of this assumption was clarified.

The well-established model for the electrical conductivity of charge carriers in ion-conducting crystalline solids is based on the random walk theory for diffusivity and the Nernst–Einstein

---

[a] Nanostructures Research Laboratory, Japan Fine Ceramics Center, Nagoya 456-8587, Japan. E-mail: t_ogawa@jfcc.or.jp

[b] Office of Institutional Advancement and Communications, Kyoto University, Uji, Kyoto 611-0011, Japan

[c] Institute of Materials Structure Science, High Energy Accelerator Research Organization (KEK), Ibaraki 319-1106, Japan

[d] Institute of Engineering Innovation, The University of Tokyo, Tokyo 113-8656, Japan

† Electronic supplementary information (ESI) available. See DOI: https://doi.org/10.1039/d4ta05684a

relation connecting mobility and diffusivity.[18] The total conductivity (σ) caused by contributions from charge carrier species (i) is expressed by $\sigma = \sum_i q_i N_i \tilde{\mu}_i$, where q_i, N_i and $\tilde{\mu}_i$ denote the charge, concentration and mobility of species i, respectively. Charge carriers are predominant charged point defects that are thermodynamically created in an ionic conductor, for example, oxide-ion vacancies ($V_O^{\bullet\bullet}$) or interstitial oxide ions (O_{int}'') in oxide-ion conductors. These point defects diffuse through the hopping of ions from one site to the next sites; therefore, to identify defects that contribute to the ionic diffusivity is necessary. The mobility of defects is related to their diffusivity (D_i), which is calculated as $\tilde{\mu}_i = q_i D_i / k_B T$, leading to $\sigma = \sum_i {q_i}^2 N_i D_i / k_B T$. When the diffusivity and concentration of defects are simply replaced by Arrhenius-type expressions, $D_i = D_{0,i}\exp(-E_{mig,i}/k_B T)$ and $N_i = N_{0,i}\exp(-E_{def,i}/k_B T)$, conductivity is rewritten as follows:

$$\sigma = \sum_i \frac{{q_i}^2 N_{0,i} D_{0,i}}{k_B T} \exp\left(-\frac{E_{def,i} + E_{mig,i}}{k_B T}\right). \tag{1}$$

Eqn (1) can also be expressed in the form of $\sigma = \sigma_0 T^{-1}\exp(-E_a/k_B T)$. The activation energy of the conductivity (E_a) is equal to the sum of formation and migration barrier energies of the mobile defect i, that is, $E_a = E_{def,i} + E_{mig,i}$. Between these two terms, the formation energy is frequently ignored in studies of ionic conductors because "the number of mobile charge carriers is extremely large".[19] Based on the assertion, identifying migration paths and estimating barrier energies have been a central topic in investigations on ion conduction. By contrast, relatively few studies have reported the behaviours of defect concentrations, for example, by performing classical molecular dynamics (MD) simulations.[20]

First-principles calculations based on the density functional theory (DFT) have become the major theoretical tool to investigate ionic conduction. In particular, first-principles MD (FPMD) simulations and nudged elastic band (NEB) methods are frequently employed. Although NEB calculations are used to determine the migration energy ($E_{mig,i}$), FPMD simulations cause the diffusivity of atoms from the trajectories in association with the activation energy (E_a) without any apparent assumption on defect structures except for composition and initial atomic configuration. Despite short sampling times and limited cell size of typical FPMD simulations, these limitations have been recently addressed by exploiting machine-learning force fields (MLFFs).[21] In contrast, point-defect concentrations under thermal equilibrium can be calculated,[22,23] on a solid foundation of the methodology for calculating defect formation energy.[24,25] Although the use of point-defect calculations for ion-conducting materials has been reported in the literature,[26–30] it remains unclear how these calculations aid in elucidating the role of point-defect formation within the ionic conduction mechanism.

In this work, the largely enhanced F-ion conductivity in BaF_2–CaF_2 solid-solution systems with a fluorite crystal structure ($Fm\bar{3}m$),[31–35] was readdressed using DFT calculations. Although the BaF_2 and CaF_2 phase diagram indicates a phase-separation behavior below 1150 K,[36] metastable nanoparticles with atomic-scale cation mixing have been prepared by high-energy ball milling[31–34] and thermal plasma.[35] The $Ba_{1-x}Ca_xF_2$ samples have exhibited a convex shape with the composition dependence of electrical conductivity (convex upward) and activation energies (convex downward) with extrema at $x = 0.5$.[32,33]

The reported conductivity of $Ba_{0.5}Ca_{0.5}F_2$ is higher by about five and two orders of magnitude than the values for the CaF_2 and BaF_2 nanoparticles, respectively.[33] There are various known F-ion solid electrolytes with higher conductivity than $Ba_{0.5}Ca_{0.5}F_2$, with β-$PbSnF_4$ exhibiting the highest conductivity.[37–39] Most of those contain elements with relatively high reduction potentials of the metal fluorides, such as Pb, Sn and Bi, compromising the electrochemical stability required for high-performance F-ion batteries.[5,6] From the viewpoint of high electrochemical stability, fluorides with tysonite and fluorite structures, composed of elements with low reduction potential, such as rare-earth and alkaline-earth metals,[37] have attracted attention as potential candidates for F-ion electrolytes. Among tysonite-type fluorides, Ba-doped LaF_3 is known to exhibit the highest conductivity, exceeding 10^{-4} S cm^{-1} at around 300 K for single-crystalline samples,[37,40,41] and disperse into a lower conductivity range compared to the single-crystalline values for polycrystalline samples.[37,41,42] In this case, aliovalent cation doping effectively generates mobile F-ion vacancies ($V_F^{\bullet}$) due to the charge balance,[40] and the material is often employed as the solid electrolyte in electrochemical cells.[5,6,42] Among the fluorite-type fluorides composed of relatively base metals, both $Ba_{0.5}Ca_{0.5}F_2$ and La-doped BaF_2 ($Ba_{0.6}La_{0.4}F_{2.4}$) exhibit a relatively high ionic conductivity in the order of 10^{-5} S cm^{-1} at 400 K.[38,43] Although these values are lower than those of tysonite-type Ba-doped LaF_3, a recent study has shown that $Ba_{0.5}Ca_{0.5}F_2$ can be used as an ion-conducting additive in the CuF_2 composite electrode.[44] While the concentration of interstitial F atoms (F_{int}') increases due to the aliovalent doping in La-doped BaF_2, no additional charged defects are formed in $Ba_{0.5}Ca_{0.5}F_2$ with respect to the charge balance. The latter isovalent cation mixing on the atomic scale has been harnessed not only in AF_2 systems (A = Ca, Sr, Ba, Cd, Pb),[31–34,38,45–48] but also in other various crystalline systems such as $(La,Sc)F_3$,[49] $Li_3In(Br,Cl)_6$,[50] $Na_3(P,As)S_4$[51] and $Gd_2(Ti,Zr)_2O_7$.[9] Therefore, the interpretation of the conductivity enhancement in BaF_2–CaF_2 solid solutions would facilitate the rationalized design of ionic conductors following a similar strategy.

The impact of nanocrystallization on the ionic conductivity of CaF_2 and BaF_2 has been clearly demonstrated through comparison with single-crystal[52] and microcrystalline samples,[31,53] where introduction of grain boundaries is attributed to the enhancement of F-ion diffusivity in the nanocrystalline samples. As for $(Ba,Ca)F_2$ mixed phases, although single-crystal or microcrystalline forms have not been synthesized, the enhanced conductivity is attributed to the diffusion of F ions in the bulk regions, involving atomic-scale mixing, as evidenced by X-ray diffraction (XRD), nuclear magnetic resonance (NMR)[31–34,53] and neutron diffraction.[35] This is further supported by the enhanced conductivity observed in single-crystal $Ca_{1-x}Sr_xF_2$ with the fluorite structure.[45,54] The enhancement of the conductivity in (Ba,Ca)F_2 mixed phases was attributed to the changes in migration energies,[32] which was theoretically investigated by classical MD simulations of nanoparticle models containing grain boundaries.[33] In contrast, NMR spin-lattice relaxation study has suggested that the prefactor part in the Arrhenius relation, which is determined by the number of mobile spins, the attempt frequency and entropy effects, contributes to the enhancement of conductivity.[34] To the best of our knowledge, no studies have elucidated the conduction mechanism of the (Ba,Ca)F_2 mixed phases based on DFT.

First, we examine the energetic stability and volumes of $Ba_{1-x}Ca_xF_2$ by performing exhaustive configuration search, and then point-defect concentrations for the mixed structure with a composition of $x = 0.5$ were investigated and compared with those of the unmixed phases, BaF_2 and CaF_2. MD simulations combined with MLFFs were used to obtain the activation energy of the mixed phase, and the migration energies of the defects in BaF_2 and CaF_2 were calculated by using the NEB method. The obtained activation and associated energies were analyzed and discussed. Then, the stability of F-related defects between AF_2 crystals was compared to investigate the effect of cation mixing on the fluorite-structured system and examine the stability in $Ba_{0.5}Ca_{0.5}F_2$.

2 Calculation methods

All electronic structure calculations were performed using the projector augmented wave (PAW) method within the DFT framework, as implemented in the VASP code.[55,56] For the exchange-correlation functional, PBEsol was used.[57] The cutoff energy was set to 550 eV when the lattice parameters and atomic coordinates were relaxed simultaneously and to 410 eV when only atomic coordinates were relaxed. The convergence criterion for the forces on atoms during a structural relaxation was set to less than 0.02 eV $Å^{-1}$.

In the exhaustive configuration search of $Ba_{1-x}Ca_xF_2$, all symmetrically inequivalent configurations for cells with up to 10 cations were produced using the CLUPAN tool,[58] yielding 1622 configurations in total. In this case, a Γ-centered *k*-point grid with spacing smaller than 0.3 $Å^{-1}$ was adopted for the Brillouin zone (BZ) integration. The formation energy and excess volume of the relaxed structures were analyzed.

Concentrations of isolated point defects were computed on the basis of the defect formation energies *via* point-defect equilibrium calculations, as described elsewhere in detail.[23] A defect species with charge $q(D^q)$ could correspond to a mobile species represented by i above when the migration energy is low enough to move. The defect formation energy ($E_{\text{def}}(D^q)$) is defined as follows:[24]

$$E_{\text{def}}(D^q) = E(D^q) - E^0 + \Delta E_{\text{c}} - \sum_{\alpha} \Delta n_{\alpha}(D^q)\mu_{\alpha} + q\mu_{\text{e}}, \quad (2)$$

where $E(D^q)$ and E^0 are the DFT energies of supercells including D^q defects and without any defects, respectively. ΔE_{c} is a correction term required for charged point defects, where the extended FNV-scheme was applied.[59,60] $\Delta n_{\alpha}(D^q)$ is the change in the number of α atoms when creating the defect. μ_{α} and μ_{e} are the chemical potentials of α atoms and electrons, respectively. As already shown, the point-defect concentration ($N_{\text{def}}(D^q)$) is approximately expressed by $N_{\text{def}}(D^q) = N_{\text{site}} \exp(-E_{\text{def}}(D^q)/k_{\text{B}}T)$, where N_{site} is the concentration of the lattice site occupied by D^q. The crystal containing charged point defects should maintain macroscopic electrical balance and satisfy the charge neutrality conditions as follows:

$$\sum_{D^q} qN_{\text{def}}(D^q) + N_{\text{h}} - N_{\text{e}} = 0. \quad (3)$$

Here, N_{h} and N_{e} are the concentrations of holes and free electrons, respectively, which are calculated from the density of states of the pristine cell. The charge neutrality condition enables the determination of the μ_{e} value for given μ_{α}.

In this work, the chemical potential of the F atom, μ_{F}, is set to be the energy of an equilibrium reaction (activity) between metal (M) and metal fluorides (MF_n), corresponding to the theoretical electrode potential of fluoride-ion batteries.[37] The chemical potential for the Pb/PbF_2 reaction was taken as the reference line.[61] 2 × 2 × 2 supercell structures of the fluorite cubic unit cell including a point defect were relaxed under fixed lattice parameters of the pristine cell without defects. In the case of $Ba_{0.5}Ca_{0.5}F_2$, Ba and Ca atoms were arranged within the cell by using the special quasi-random structure (SQS) procedure,[62] as implemented in the ATAT tool.[63] The BZ integration for the supercells was performed using the 3 × 3 × 3 *k*-point grid. In this work, point-defect concentrations under thermal and charge equilibrium were calculated using the pydecs code.[23]

In measuring the difference in defect formation energy between an examined AF_2 material and BaF_2, potential offsets were calculated (see the ESI† for details on the calculation procedure). In obtaining the energy barriers of F-related defects in BaF_2 and CaF_2, the climbing-image NEB (cNEB) method[64] with three intermediate images was used. The bonding characteristics of AF_2 crystals were assessed *via* Crystal Orbital Overlap Populations (COOPs), Löwdin charges and Madelung energies by using LOBSTER.[65]

MD simulations of $Ba_{0.5}Ca_{0.5}F_2$ were performed using the on-the-fly MLFF scheme, as implemented using the VASP (ver. 6.3.2) code.[66] The time step was set to 2 fs. An on-the-fly MLFF was trained using the same 2 × 2 × 2 supercell as that used for the point-defect calculations, with NPT-ensemble MD combined with Langevin thermo-barostat.[67] The training MD was performed by increasing the temperature from 300 K to 1500 K within 80 ps, followed by a short low-temperature MD run (for 0.2 ps at $T = 10$ K). The number of collected structures in the training dataset is 923 and the numbers of basis sets for Ba, Ca and F-atoms are 439, 839 and 4315, respectively. The root-mean squared errors in energies, forces and stress tensors of the generated MLFF are 1.02 meV per atom, 0.042 eV $Å^{-1}$ and 0.45 kbar, respectively.

In obtaining diffusivity, MD calculations with the prepared MLFF were performed using a 4 × 4 × 4 supercell, including 768 atoms with cation configurations determined using the SQS scheme. The examined temperatures ranged from 600 K to 1000 K in increments of 100 K. First, NPT-ensemble MD simulations were performed to determine the lattice constants at each temperature (Fig. S1†). Using the obtained lattice constants, NVT-ensemble MD simulations were performed with Nosé-thermostat.[68] After annealing for 100 ps, trajectories were gathered at every 20 fs for 500 ps. The accuracy of the adopted MLFF was rechecked for structures after annealing at each temperature, and it was found to meet the acceptable level (Fig. S2†). Mean square displacement (MSD) was calculated by averaging over atoms and different initial times with a maximum lag time of 300 ps to achieve sufficient statistical average convergence. The diffusivity of F atoms, D_F, was obtained by fitting the time-dependent MSD, MSD(t), with the Einstein relation, that is, $\mathrm{MSD}(t) = 6D_Ft$. In extracting event probability of interstitial F ions and co-generated F vacancies during MD sampling, the coordinates of each F-atom were mapped to the nearest lattice site using Voronoi tessellation.[69] Atomic configurations and density maps were represented by the VESTA code.[70]

3 Results and discussion

3.1 BaF_2–CaF_2 solid solution

The thermodynamic stability of $Ba_{1-x}Ca_xF_2$ solid solutions was examined by the exhaustive configuration search which is used to evaluate the phase stability of the mixed phases and to discover possible ordered structures. Fig. 1a shows the formation energies measured from the composition-weighted average of the end-member energies. In the case of $T = 1200$ K, composition-dependent configuration entropy term ($-TS_{\mathrm{config}}$) was added, where $S_{\mathrm{config}} = -k_B(x\ln x + (1-x)\ln(1-x))$. The results indicate a phase separation tendency, even though the tendency decreases at higher temperature. The metastability of the cation-mixed phases is consistent with the reported experimental behavior.[31,33] The mechanochemically synthesized mixed phases were decomposed above 700 K, where cation diffusion is sufficiently activated. The calculated formation energy surpasses 0.15 eV per cation or 14.5 kJ mol^{-1}, at around $x = 0.5$. Similar values have been observed in oxides; for example, the formation energy of fluorite-structured $Ce_{1-x}Zr_xO_2$ is approximately 15 kJ mol^{-1} at $x = 0.5$.[71] In this oxide system, miscibility is observed at high temperatures, for example, above 1800 K at $x = 0.5$.[72] Although our calculations show the phase separation behavior even at a high temperature of 1200 K, mixed phases were observed at temperatures above 1150 K over the entire composition range in the experimental phase diagram.[36] Our calculations overestimate the transition temperature from a two-phase separation state to a single solid-solution state probably because our calculations do not include vibrational contributions. A similar overestimation was found in a previous calculation study on $Ce_{1-x}Zr_xO_2$.[73]

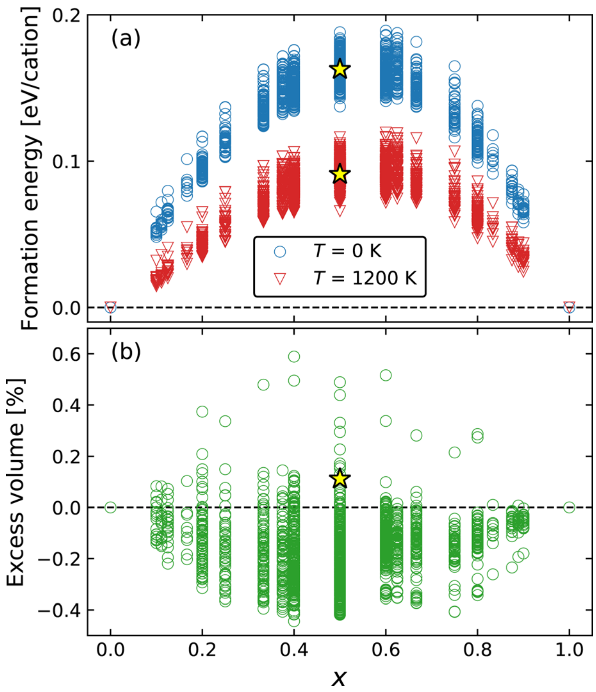

Fig. 1 (a) Formation energies at $T = 0$ and 1200 K and (b) excess volume of $Ba_{1-x}Ca_xF_2$ solid solution as a function of composition, x. The yellow star symbols indicate the values of the SQS model with a 2 × 2 × 2 conventional supercell.

The excess volume, which is a relative volume with respect to the composition-weighted average of the BaF_2 and CaF_2 volumes, is shown in Fig. 1b, exhibiting a small deviation to negative (contraction) and positive (expansion) directions with absolute values lower than 0.6%. Therefore, Vegard's law is almost satisfied in the mixed system. Determining the lattice constants of the mixed phase is experimentally difficult because of the broadening of the XRD peaks, although Düvel *et al.* reported the expansion tendency with an excess volume reaching 1.5–1.7% at around $x = 0.3$–0.5.[33] In our exhaustive calculations, the examined cells include up to 10 cations, inevitably forming structures with a short-range order compared to a more realistic random structure available in a larger cell. However, the excess volume of a random structure would lie in the dispersion of the searched results because such a dispersed range may include two opposite extreme cases toward contraction and expansion.

Fig. 2a shows the relaxed random structure prepared using the SQS scheme for $Ba_{0.5}Ca_{0.5}F_2$, including 96 atoms (32 cations), where the interstitial positions are represented as the ideal fluorite crystal before relaxation. Fig. 2b shows the frequency of the combination of coordinating cations around 64 F-atom sites (8c) and 32 interstitial sites (4b) in the cell, where the 8c and 4b sites have tetrahedral and octahedral coordination, respectively, as represented in the insets of Fig. 2b. In the prepared model, the coordination environments around F-atom sites are almost fully random. The corresponding probability distribution around ^{19}F-atoms determined by NMR for ball-milled samples has shown a slight deviation from the values of the ideal random distribution; thus, the frequencies of Ca_3Ba and $CaBa_3$ coordination patterns were larger and smaller than the ideal values, respectively.[33] However, Breuer and Silkening reported that such differences in the local environment do not significantly affect the long-range conduction of F$^-$ ions through measurements of samples prepared at different ball-milling times.[34] Therefore, the random structure model can capture the relationship between ionic conductivity and local structures.

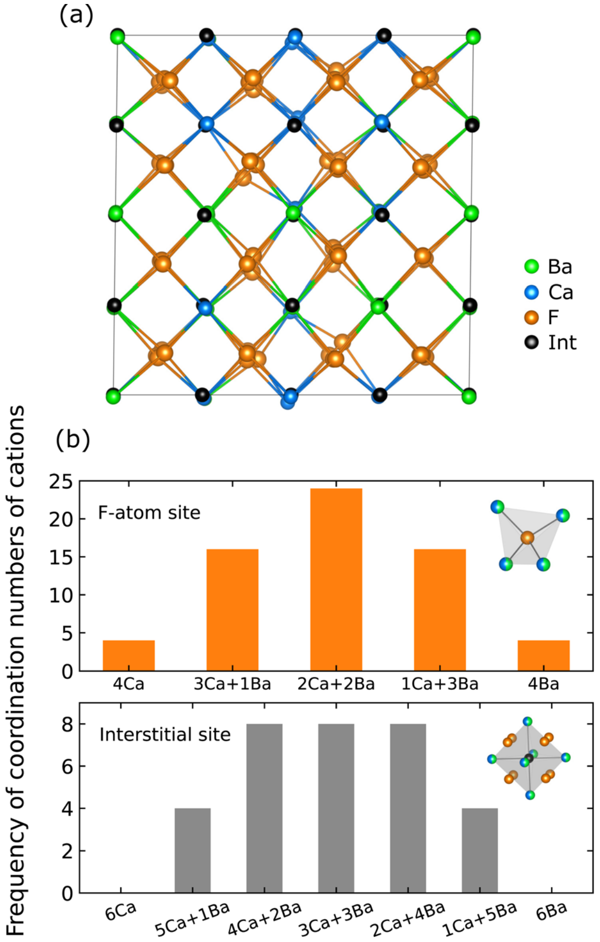

Fig. 2 (a) Relaxed SQS structure in the 2 × 2 × 2 conventional supercell of $Ba_{0.5}Ca_{0.5}F_2$ and (b) histogram of the combination of coordinating cations around the F-atom sites (8c) and interstitial sites (4b) in the fluorite supercell.

The formation energy and excess volume of the SQS structure are shown in Fig. 1. Considering that the energy of the SQS structures is located in the middle of the energy dispersion obtained from the exhaustive search, the phase separation tendency is reconfirmed for the random structure in the larger cell. Structural relaxation induces local displacements from the ideal lattice sites (Fig. 2a). The observed excess volume expansion accounts for approximately 0.1%, which is relatively small compared with an experimental value of approximately 1.5%.[33] In our calculations, the diffusivity of F ions can be affected by local structural distortion rather than the minute volume expansion.

3.2 Point-defect calculations of BaF_2–CaF_2 solid solution

In determining the possible range of the chemical potential of the F atom (μ_F), μ_F values are calculated for various metal/metal-fluoride equilibrium reactions (M/MF_n) as summarized in Fig. S4.† Cu/CuF_2 has the highest potential among the examined cases in our calculations except for noble material series, and it has recently attracted considerable attention as a promising active cathode material for fluoride-ion batteries.[44,74,75]

Considering that fluorides with low equilibrium μ_F are more stable during electrochemical reactions, the fluorides of alkali and alkaline earth metals, including BaF_2 and CaF_2, are preferred as an electrolyte with a high electrochemical stability, which would allow the stable use of the $(Ba,Ca)F_2$ phase in the composite electrode.[44] In the following point-defect calculations, μ_F is swept between the values for Li/LiF and Cu/CuF_2.

The concentrations of point defects in BaF_2, CaF_2 and $Ba_{0.5}Ca_{0.5}F_2$ were examined under thermal and charge equilibrium. For BaF_2 and CaF_2, the vacancies and interstitials of F and each cation (Ba or Ca) were evaluated, where the chemical potential of each cation is determined from the energy of the host material and μ_F. The resulting concentrations at $T = 600$ K are plotted in Fig. 3a and b, respectively. In this figure, the horizontal axes show variation of μ_F relative to the value at the equilibrium of Pb/PbF_2. In both materials, the concentrations of cation-related defects are low; thus, they are not shown in the panels, and the predominant defects are the anion Frenkel pair, namely, positively charged F-vacancies ($V_F^{\bullet}$) and negatively charged interstitial F-atoms (F_{int}').

Based on the above examination for the unmixed compounds, for the $Ba_{0.5}Ca_{0.5}F_2$ case, F vacancies ($V_F{}^q$, $q = +, 0$) and interstitial F atoms ($F_{int}{}^q$, $q = -, 0$) were considered at each lattice site in the SQS cell shown in Fig. 2a. The obtained defect concentrations at each site are summed up within each defect type. The resulting concentrations at 600 K are plotted in Fig. 3c, indicating the higher concentrations of the predominant anion Frenkel pair by several orders of magnitude than those in CaF_2 and BaF_2.

The dependence of the $V_F^{\bullet}$ concentration (which is identical to that of F_{int}') for the examined compounds is plotted as a function of inverse temperature (Fig. 4). Here, μ_F was set to the base value of Pb/PbF_2, where the Frenkel pair is predominant in the examined temperature range. The defect concentrations in $Ba_{0.5}Ca_{0.5}F_2$ are higher than those in unmixed compounds over the whole examined temperature range, and all lines exhibit constant gradients. Fitting the lines with the Arrhenius equation yields a nominal formation energy equivalent to half of the Frenkel-pair formation energy. For BaF_2 and CaF_2, the extracted values are 0.93 and 1.25 eV, which are almost identical to the defect formation energies evaluated from the point-defect equilibrium calculations. For the $Ba_{0.5}Ca_{0.5}F_2$ case, the formation energy obtained from the fitting is 0.18 eV. The corresponding single value cannot be obtained from the point-defect equilibrium calculations because various defects at different lattice sites simultaneously contribute to the summed-up concentrations. Notably, not only an aliovalent dopant but also an isovalent dopant with a large difference in ionic size can remarkably increase charge carrier defects.

3.3 MD simulations of $Ba_{0.5}Ca_{0.5}F_2$

Using MLFF-MD simulations at 600 to 1000 K, radial distribution functions (RDFs) and diffusion properties of F ions in $Ba_{0.5}Ca_{0.5}F_2$ are analyzed. The RDFs are plotted separately for pairs between the F atom and each constituent element, as shown in Fig. 5. The first peaks in the RDFs for the F–Ca pair

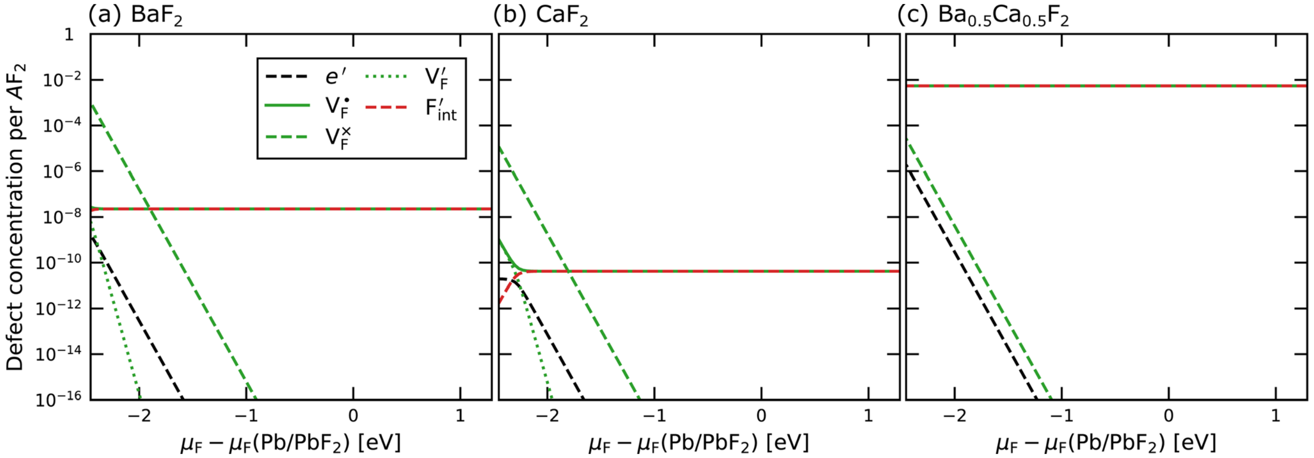

Fig. 3 Point-defect concentrations as a function of μ_F at $T = 600$ K for (a) BaF_2, (b) CaF_2 and (c) $Ba_{0.5}Ca_{0.5}F_2$. The lower and upper μ_F values in the horizontal axis correspond to the equilibrium μ_F values for Li/LiF and Cu/CuF_2, respectively.

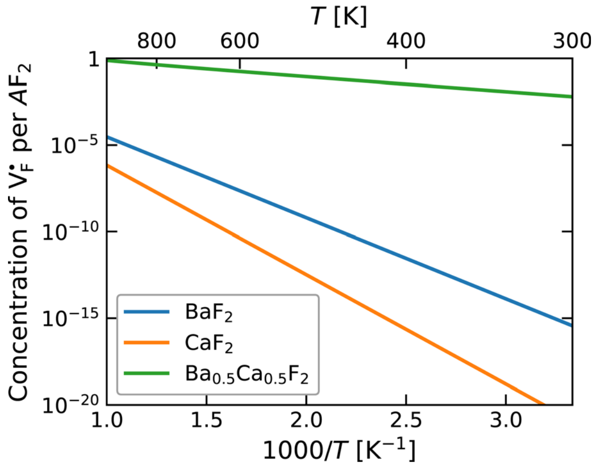

Fig. 4 Point-defect concentrations as a function of temperature, where μ_F is fixed to be the value for Cu/CuF_2. Under these conditions, anion Frenkel pairs are dominant.

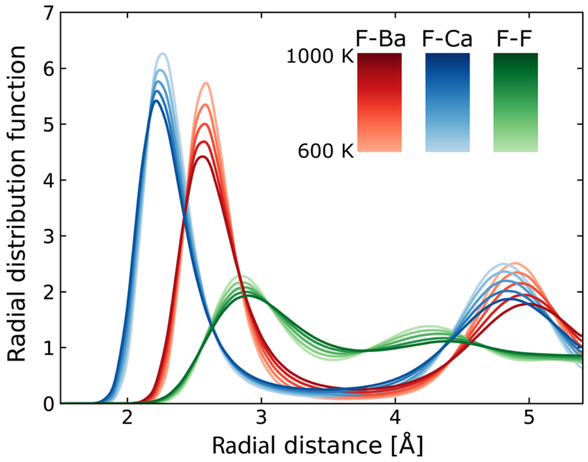

Fig. 5 Radial distribution functions around F atoms in $Ba_{0.5}Ca_{0.5}F_2$.

appear at around 2.2 Å, which is shorter by about 0.3 Å than that of the F–Ba pair. These reflect the difference in the ionic radii (1.56 and 1.26 Å for Ba^{2+} and Ca^{2+} ions with eight coordination, respectively[76]) and coincide with the tendency of the lattice constants of BaF_2–CaF_2 solid solutions, which almost follows Vegard's law. The RDFs of the F–F pair have weaker and broader first peaks at a position farther than that of the first peaks of cations. All peaks in the RDFs weaken with the increase in temperature, reflecting the increased movement of atoms, but no significant changes in shape and no additional peaks are observed.

The MSD of F atoms, which is plotted in Fig. 6a, shows usual ballistic and diffusive behaviors;[77] The time evolution is proportional to t^2 in the relatively short time range less than 0.1 ps and to t^1 in the longer time range. During the simulations, no hopping diffusion of the cations was observed, indicating that the structural changes towards phase separation hardly occur without any cation defects in simulations, whereas the phase separation was observed at temperature above 700 K in experiments.[33] Even in classical MD simulations of BaF_2–CaF_2 nanoparticles, including surfaces, grain boundaries and potential cation defects, apparent phase separation was not observed at 1200 K,[33] which is consistent with our DFT-based MD simulations at temperatures below 1000 K.

The diffusion coefficients (D_F) extracted from the MSDs are plotted as a function of inverse temperature, as shown in the inset of Fig. 6a. We evaluated the standard deviations in the averaging of D_F using the MD2D package,[78] resulting in relative deviations of less than 6%, which is smaller than the size of the data points shown in the inset. The linear fit with the Arrhenius equation provides an activation energy (E_a) of 0.42 eV for F-atom diffusion. This value corresponds to the sum of the contributions from defect formation and migration as in the explicit formalism of the conductivity in eqn (1). The theoretical ionic conductivity (σ) below 500 K is obtained from extrapolated D_F at higher temperatures than 600 K *via* the relation $\sigma = e^2 N_F D_F / k_B T$, where N_F denotes the concentration of F-atom lattice sites. The calculated σ values are compared with the experimental data

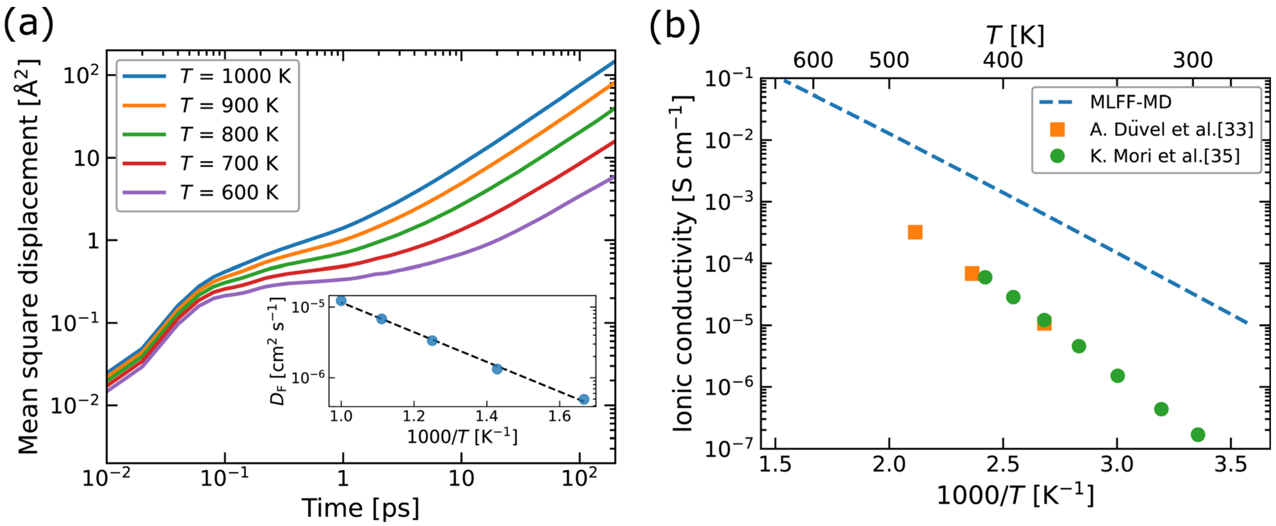

Fig. 6 (a) Mean square displacement (MSD) as a function of time and (b) ionic conductivity as a function of 1000/*T*, for F atoms in $Ba_{0.5}Ca_{0.5}F_2$. In the inset of (a), diffusion coefficients (D_F) obtained by fitting the MSDs are plotted. In (b), the experimental values for $Ba_{1-x}Ca_xF_2$ with $x \sim 0.5$ (ref. 33 and 35) are plotted for comparison.

extracted from the literature,[33,35] as shown in Fig. 6b, which indicates that the theoretical results overestimate the experimental ones by about 1–2 orders of magnitude. We consider that two factors may contribute to the observed differences. The first factor is the possible existence of a superionic-like phase transition, associated with a change in mobile defect species and/or the formation of defect complexes, as reported for α-Li_3N.[79] Although we also calculated the MSDs at $T = 300$, 400 and 500 K, the linear dependence of the MSDs on simulation time could not be achieved within the MD sampling time. The elucidation of low-temperature diffusion properties would require longer simulation times and more careful examinations of the convergence, both of which are beyond the scope of this study. The second factor is the retarding effect at grain boundaries in nanoparticles on the conductivity in the experiments, as reported for Y-doped ZrO_2 (ref. 80) and tysonite-type Ba-doped LaF_3,[41] though for the latter case, it has also been reported that the effect of grain boundaries could be suppressed by optimizing the microstructure.[37]

In confirming the temperature dependence of the concentrations of F-atom point defects contributing to ionic diffusion, the time evolution of spontaneously formed F-atom defects was extracted and analyzed from the MD trajectories. Fig. 7a shows the distribution of F atoms at $T = 1000$ K, which was generated by contracting the F-atom trajectories into the unit cell. As shown in the figure, although F-atoms reside predominantly at the 8c site, their distribution is also present at the interstitial 4b sites. In extracting the sojourn time of F atoms on the interstitial sites, the existing probability of F atoms at the site was calculated for each snapshot, and the time-series data were averaged, by using the Voronoi-tessellation mapping of F-atom coordinates onto the closest lattice site. The probability represents the concentrations of interstitial F-atoms, which are equivalent to those of F-vacancies. The obtained probabilities at each temperature are plotted in Fig. 7b as a function of inverse temperature. By fitting the data with the Arrhenius equation, the defect formation energy extracted from the MD simulations is 0.12 eV, which is close to that from the point-defect calculations (0.18 eV). The slight difference may be attributed to finite-

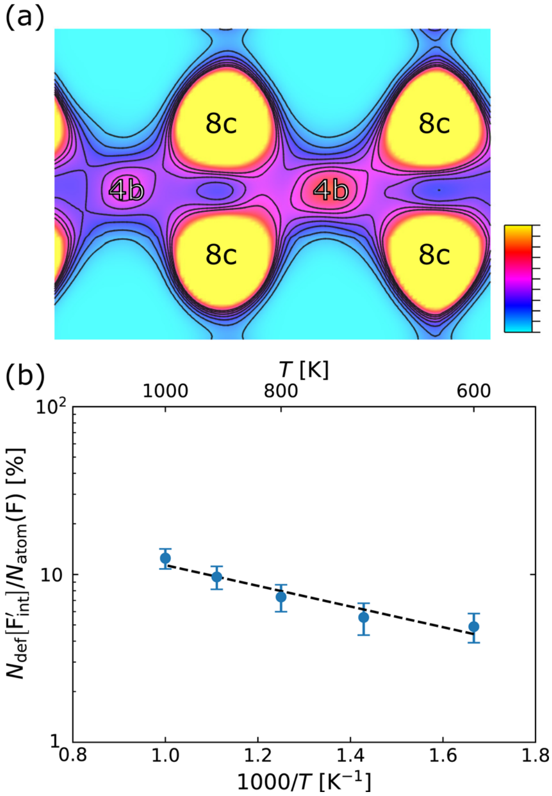

Fig. 7 (a) Distribution of F-atoms on the (110) plane at $T = 1000$ K, where F-atom trajectories in the supercell are contracted into a unit conventional cell. (b) Extracted and averaged existence probability of F-atoms on the interstitial sites.

temperature effects such as lattice vibration, thermal expansion and the clustering (association) of point defects, which are ignored in the above-mentioned point-defect calculations. The findings indicate that the approach of point-defect chemistry provides direct access to the defect formation energy that comprises the activation energy.

3.4 Comparison of activation energies

In comparing the activation energies, the migration energies of $V_F^\bullet$ and F_{int}' in CaF_2 and BaF_2 were calculated using the cNEB method, because the F-ion diffusivity of these compounds is too small to achieve statistical convergence during MD simulations without extrinsic dopants. In the case of $V_F^\bullet$, an F-ion neighboring to a vacancy site migrates to the vacancy site (Fig. 8c). In the case of F_{int}', the interstitialcy diffusion path involving the movement of the neighboring F-atom at the 8c site is examined because the direct migration pathway to the next interstitial site could not be defined (Fig. 8d). Fig. 8a and b show the calculated relative energies on the migration paths, and the obtained saddle-point energies (E_{mig}) are summarized in Table 1. As shown in the table, the barriers for $V_F^\bullet$ in BaF_2 and CaF_2 are lower by about 0.2 and 0.3 eV, respectively, than those for F_{int}'. These results indicate that $V_F^\bullet$ is more mobile than F_{int}' in BaF_2 and CaF_2.

All the energies, associated with the activation energy of ionic conductivity, are summarized in Table 1. The activation energies for BaF_2 and CaF_2 were derived by summing the formation and migration energies for F-vacancies *via* the relation: $E_a = E_{def} + E_{mig}$. Meanwhile, the migration energy for F-ion defects in $Ba_{0.5}Ca_{0.5}F_2$ was calculated by subtracting the formation energy from the activation energy ($E_{mig} = E_a - E_{def}$). As previously mentioned, the $Ba_{0.5}Ca_{0.5}F_2$ model was constructed on the basis of the SQS scheme. In this model, various nonequivalent migration paths are observed; thus, comprehensive determination of the migration energy by NEB calculations is not feasible. The obtained E_a value shows a large difference between the mixed and unmixed phases, accounting for approximately 1 eV. As shown in Table 1, the E_{mig} values of $V_F^\bullet$ in the BaF_2 and CaF_2 are comparable to that of $Ba_{0.5}Ca_{0.5}F_2$. The differences in the migration barrier among the fluorides are less than 0.15 eV. Therefore, the differences in the E_a value should be largely attributed to the difference in the defect formation energy.

Table 1 Defect formation energies, E_{def}; migration barriers, E_{mig}; and activation energies, E_a; in comparison with experimental activation energies

	BaF_2	CaF_2	$Ba_{0.5}Ca_{0.5}F_2$
E_{def}	0.93	1.25	0.18
$E_{mig}(V_F^\bullet)$	0.38	0.27	0.24[a]
$E_{mig}(F_{int}')$	0.55	0.55	
$E_a^{Calc.}$	1.31[a]	1.44[a]	0.42
$E_a^{Expt.}$	2.15[b]	1.32[b]	0.62[f]
	1.49[c]	1.88[d]	0.53[g]
	1.64[e]	2.13[e]	

[a] Calculated *via* the relation: $E_a = E_{def} + E_{mig}$. [b] Ref. 81. [c] Ref. 82. [d] Ref. 83. [e] Ref. 84. [f] Ref. 32. [g] Ref. 33.

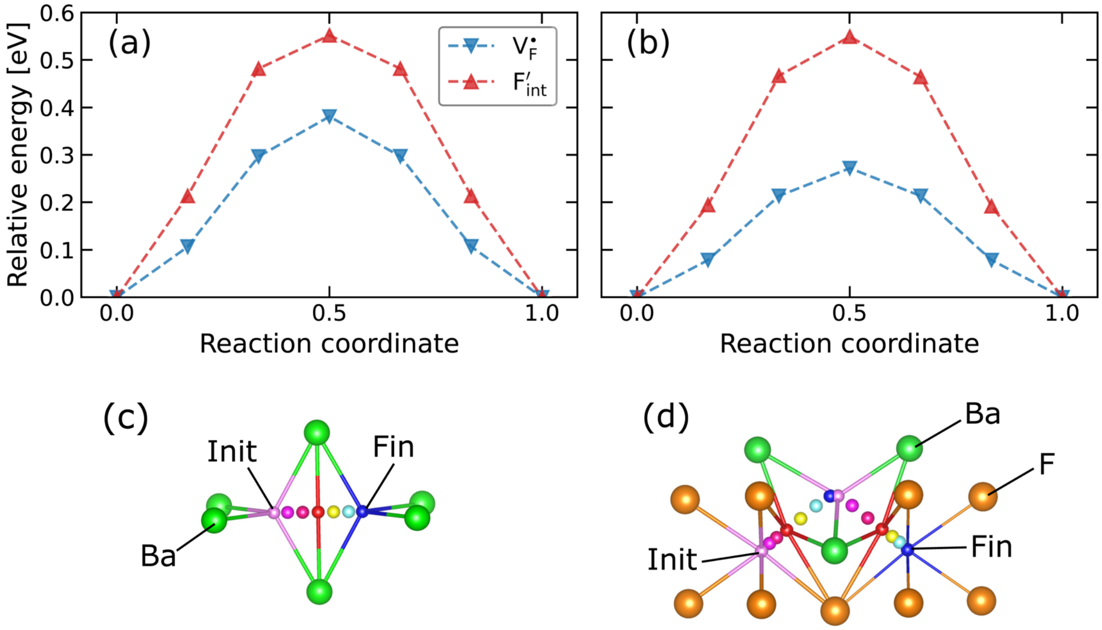

Fig. 8 Relative energies on the migration paths of $V_F^\bullet$ and F_{int}' in (a) BaF_2 and (b) CaF_2. Atomic configurations on the paths of (c) $V_F^\bullet$ and (d) F_{int}' in BaF_2. In (c) and (d), the migrating F-atoms are represented by small spheres with various colors from the initial position (0) with pink to the final position (1) with blue, *via* the saddle point (0.5) with red, where the values in the parentheses denote the reaction coordinate. Ba and lattice F atoms are shown by green and orange large spheres, respectively. The inter-atomic bonds are depicted only for the three images at initial, saddle point, and final states.

Table 1 also lists the experimental E_a values for BaF_2 and CaF_2 bulks[81–84] and for $Ba_{1-x}Ca_xF_2$ nanoparticles at a composition near to $x = 0.5$.[32,33] The experimental values of BaF_2 and CaF_2 are dispersed in the 1.3–2.1 eV range, containing the calculated values. In contrast, the E_a value of BaF_2 and CaF_2 nanoparticles exhibits relatively low values less than 0.8 and 1.0 eV, respectively,[32,33] which would reflect particle-size effects. The experimental E_a values of the $Ba_{0.5}Ca_{0.5}F_2$ nanoparticles are in the range of 0.5–0.6 eV, which are lower than those of BaF_2 and CaF_2 nanoparticles. Although distinguishing the nanoparticle and cation mixing effects in experiments is difficult because of the absence of experiments with larger grains as already mentioned, this work provides a theoretical clue on the effects of local structural disorders induced by the cation mixing on the E_a values and F-ion transport properties of the bulk region.

If MD simulation can be performed in a large cell for sufficiently long simulation time based on reliable energy and force calculations, then it would be a suitable tool to directly compute the activation energy of mobile atoms in an ionic conductor. However, a limited computational capability promotes the use of a searching method for the saddle point on a migration path, such as the cNEB method, to obtain the migration energy (E_{mig}). Point-defect calculations can aid in the identification of dominant defect species and the estimation of defect formation energy (E_{def}). The essential role of point-defect concentrations in MD simulations is emphasized for ionic conductors such as AgI and β-PbF_2 in the review by Hull.[20] As demonstrated also in our MD simulations, when mobile ions in a crystal migrate through interstitial lattice sites or fractionally occupied sites such as vacancies, the temperature-dependent occupation probabilities can be a key factor to understand the migration behavior associated with the point-defect formation. Similar situations could arise in various solid electrolytes. For example, in sulfide-based compounds for Li-ion solid electrolytes, the Li-ion migration barrier is highly dependent on the type of anion sublattice (bcc or fcc/hcp), and the difference in the probability density of Li atoms between two sites on a Li-ion migration path is used to explain the trend of diffusivity.[11] Considering that the latter probability density is related to point-defect concentrations, point-defect calculations may provide a comprehensive understanding of the underlying transport mechanism and suggest the way to tailoring crystals with higher ionic conduction.

3.5 Comparison of point-defect formation energy

To investigate the mechanism responsible for the decrease in the defect formation energies (E_{def}) of $V_F^{\bullet}$ and F_{int}' in $Ba_{0.5}Ca_{0.5}F_2$, the difference in E_{def} between different materials was calculated. Here, we suppose that the subject material is adjacent to BaF_2 and it shares the same Fermi level (see the ESI† for details). First, we compared the relative formation energies of AF_2 series (A = Ca, Ba, Sr, Cd, Pb) with respect to the BaF_2 values (Fig. 9a). The results indicate the opposite energy alignments between $V_F^{\bullet}$ and F_{int}' except for the PbF_2 case. These trends are plotted as a function of the ionic radius (Fig. 9b), expressing systematic changes for each defect type except for PbF_2, and relatively small changes in the anion Frenkel-pair energies.

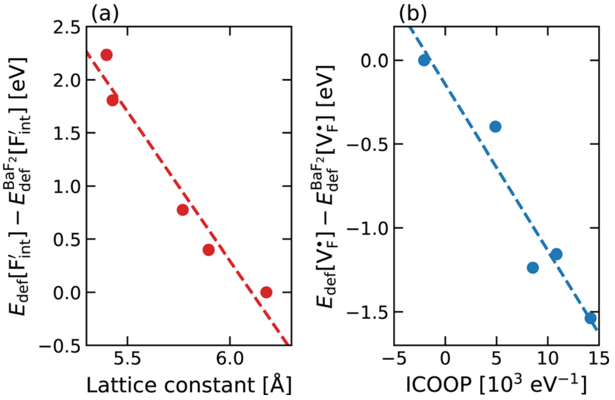

Fig. 10 Correlation plots of relative defect formation energies for (a) interstitial F ions and (b) F-ion vacancies for AF_2 (A = Ca, Ba, Sr, Cd, Pb). For the descriptors, see the main text.

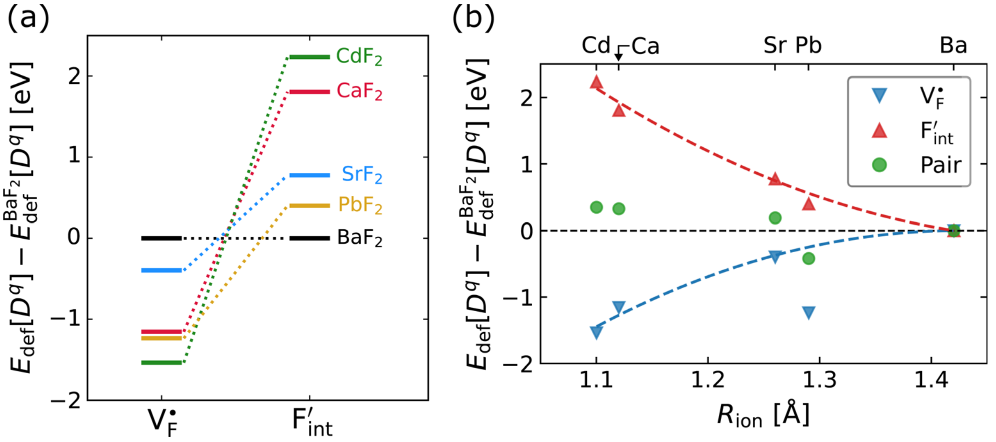

Fig. 9 (a) Comparison of the relative formation energies of $V_F^{\bullet}$ and F_{int}' of AF_2 (A = Ca, Ba, Sr, Cd, Pb) with regard to BaF_2 and (b) its dependence on the ionic radius of A^{2+} with eight coordination.[76] In (b), points for half the formation energies of the anion Frenkel pair and fitted lines with a parabolic function except for PbF_2 for guiding eyes are also shown.

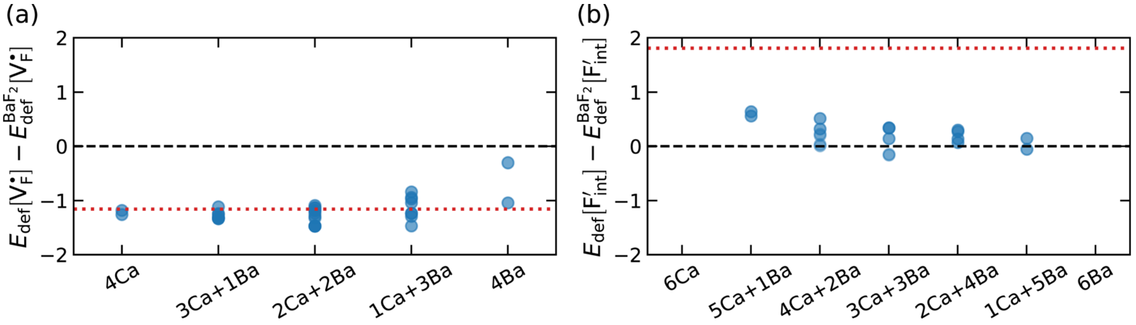

Fig. 11 Point-defect formation energies of (a) F-vacancies and (b) interstitial F-atoms in $Ba_{0.5}Ca_{0.5}F_2$, which is measured from the values in BaF_2. The red dotted lines indicate the corresponding energies for CaF_2.

In elucidating the origin of the stability trends, structural and electronic properties correlating with the relative formation energies were explored. The energetic trend for F'_{int} correlates with the lattice constants (Fig. 10a), including PbF_2. Considering that the lattice constant in the fluorite structure is linearly proportional to the bond lengths between atoms in the crystal, the relationship can be interpreted as follows: the narrower the interstitial space, the greater the repulsion between the incorporated F and surrounding atoms. In contrast to the F'_{int} case, poor correlation was observed between the relative energies for $V_F^{\bullet}$ and bond lengths or lattice constants. The bonding characteristics calculated *via* the projection of electronic states onto local atomic orbitals were examined as described in the Method section. Electrostatic properties such as Löwdin charges and Madelung energy also exhibit poor correlation (Table S1†), but integrated COOP up to the Fermi level (ICOOP) between adjacent fluorine and the cation was found to have a linear relationship, as shown in Fig. 10b. Therefore, the bonding strength represented by the COOP analysis is a key factor to capture the trend of $E_{def}(V_F^{\bullet})$, including the PbF_2 case.

The curious exceptional behavior of the defects in PbF_2 may be related to the $6s^2$ lone pair of Pb^{2+} ions. Such a lone pair strongly affects the crystal structures as well as local bonding characteristics,[85,86] electric and optical properties[87] and F-ion conductivity.[87,88] The previous DFT calculations have shown that COOP analyses reveal the bonding characteristics between Pb and neighboring anions.[85,86,89] Also in our case, the density of states and COOP of PbF_2 exhibit similar hybridization to the case of other Pb-including compounds (Fig. S5†). Therefore, ICOOP can be a good indicator of the trend of $V_F^{\bullet}$ formation energy. Although such s^2 lone pairs could enhance F-ion migrations,[88,90] materials containing Sn and Pb would require more careful application with respect to electrochemical stability than compounds composed of Ba and Ca (Fig. S4†).

The relative formation energies with regard to the BaF_2 values for 64 and 32 kinds of $V_F^{\bullet}$ and F'_{int} in the $Ba_{0.5}Ca_{0.5}F_2$ cell are shown in Fig. 11. As shown in the figure, although the dependence of the energy on the local coordination environments is unclear, the energetic stability is different between the two defects. While the relative energies of $V_F^{\bullet}$ are low and comparable to those of CaF_2, the relative energies of F'_{int} are near to those of BaF_2. Therefore, the mixed phase exhibits a behavior inconsistent with the trend in the AF_2 series. The lattice constant of the random structure scarcely expand from the average value (Fig. 1b). Thus, the decrease in the relative defect energy in the mixed phase could be attributed to the local structural disorder induced by the mixing of isovalent cations with a large ionic-radius difference. As an example, the local structures of F'_{int} are depicted in Fig. S6,† representing that the large structural changes during relaxation occur in the mixed phase in contrast to the cases of BaF_2 and CaF_2. The large changes would be allowed by distortions contained not only in neighboring atoms, but also in more distant atoms. When additional aliovalent doping is applied into the disordered structure, as reported for $(Ca,Sr)F_2$ doped with rare-earth metals,[54] higher conductivity may be achieved as a result of the altered formation of F-ion defects.

4 Conclusions

In this study, ionic conductivity enhancement in $Ba_{1-x}Ca_xF_2$ was investigated by evaluating the defect formation, migration and activation energies using point-defect calculations, migration-path searches and MLFF-MD simulations, under consistent DFT conditions. The comparison of the obtained energies for $Ba_{0.5}Ca_{0.5}F_2$, BaF_2 and CaF_2 shows that the cation mixing of Ba^{2+} and Ca^{2+} induces the reduction of the formation energies of the F-ion Frenkel pair ($V_F^{\bullet}$ and F'_{int}), rather than the migration barriers. By arranging the relative defect formation energies for AF_2 series, $V_F^{\bullet}$ and F'_{int} are found to exhibit opposite trends against ionic sizes of cations. Meanwhile, the energies of the F-ion vacancies and interstitials in $Ba_{0.5}Ca_{0.5}F_2$ deviate from the trends, and each energy is close to the lower energy between CaF_2 and BaF_2. The latter anomalous behavior is due to the local structural distortions caused by the mixing of cations with a large difference in the ionic radius. In general, aliovalent dopants are used for the production of mobile charge carriers in the field of solid-state ionics. However, our findings indicate that isovalent dopants with a different size from the constituents of host materials may enhance the ionic conductivity in a wide range of materials other than the present system. Moreover, the present research indicates that enhancement of ionic conductivity not only results from the lowering of migration barriers but also from the increase in charge carrier or point-defect concentrations and thus suggests that the point-defect chemistry can provide insights into the underlying mechanism of ion conduction in crystalline solids.

Data availability

Raw data were generated at Japan Fine Ceramics Center at Nagoya in Japan. Derived data supporting the findings of this study are available from the corresponding author T. O. on request.

Conflicts of interest

There are no conflicts to declare.

Acknowledgements

This work was supported by the "Research and Development Initiative for Scientific Innovation of New Generation Batteries (RISING3)," JPNP 21006, commissioned by the New Energy and Industrial Technology Development Organization (NEDO) and by the Ministry of Education, Culture, Sports, Science and Technology as "Program for Promoting Research on the Supercomputer Fugaku" (Computational Research on Materials with Better Functions and Durability Toward Sustainable Development, JPMXP1020230325) and also partially supported by the Japan Society for the Promotion of Science (JSPS) KAKENHI (Grant no. JP24K01173, JP22H05142 and JP22H05146) and the Iketani Science and Technology Foundation (no. 0361237-A). The computational resources of supercomputer Fugaku provided by the RIKEN Center for Computational Science (Project ID: hp230205 and hp240224) were used.

References

1 D. Larcher and J.-M. Tarascon, *Nat. Chem.*, 2015, **7**, 19–29.
2 J. C. Bachman, S. Muy, A. Grimaud, H.-H. Chang, N. Pour, S. F. Lux, O. Paschos, F. Maglia, S. Lupart, P. Lamp, L. Giordano and Y. Shao-Horn, *Chem. Rev.*, 2016, **116**, 140–162.
3 Y. Zhang, R. Knibbe, J. Sunarso, Y. Zhong, W. Zhou, Z. Shao and Z. Zhu, *Adv. Mater.*, 2017, **29**, 1700132.
4 W. Zhang and Y. H. Hu, *Energy Sci. Eng.*, 2021, **9**, 984–1011.
5 M. A. Nowroozi, I. Mohammad, P. Molaiyan, K. Wissel, A. R. Munnangi and O. Clemens, *J. Mater. Chem. A*, 2021, **9**, 5980–6012.
6 S. V. Gopinadh, P. V. R. L. Phanendra, B. John and T. D. Mercy, *Sustainable Mater. Technol.*, 2022, **32**, e00436.
7 B. C. Wood, J. B. Varley, K. E. Kweon, P. Shea, A. T. Hall, A. Grieder, M. Ward, V. P. Aguirre, D. Rigling, E. L. Ventura, C. Stancill and N. Adelstein, *Philos. Trans. R. Soc., A*, 2021, **379**, 20190467.
8 Z. Zhang and L. F. Nazar, *Nat. Rev. Mater.*, 2022, **7**, 389–405.
9 K. J. Moreno, G. Mendoza-Suárez, A. F. Fuentes, J. García-Barriocanal, C. León and J. Santamaria, *Phys. Rev. B: Condens. Matter Mater. Phys.*, 2005, **71**, 132301.
10 E. Kendrick, J. Kendrick, K. S. Knight, M. S. Islam and P. R. Slater, *Nat. Mater.*, 2007, **6**, 871–875.
11 Y. Wang, W. D. Richards, S. P. Ong, L. J. Miara, J. C. Kim, Y. Mo and G. Ceder, *Nat. Mater.*, 2015, **14**, 1026–1031.
12 N. Adelstein and B. C. Wood, *Chem. Mater.*, 2016, **28**, 7218–7231.
13 X. He, Y. Zhu and Y. Mo, *Nat. Commun.*, 2017, **8**, 15893.
14 X. Yang, A. J. Fernández-Carrión, J. Wang, F. Porcher, F. Fayon, M. Allix and X. Kuang, *Nat. Commun.*, 2018, **9**, 4484.
15 D. Di Stefano, A. Miglio, K. Robeyns, Y. Filinchuk, M. Lechartier, A. Senyshyn, H. Ishida, S. Spannenberger, D. Prutsch, S. Lunghammer, D. Rettenwander, M. Wilkening, B. Roling, Y. Kato and G. Hautier, *Chem*, 2019, **5**, 2450–2460.
16 K. Jun, Y. Sun, Y. Xiao, Y. Zeng, R. Kim, H. Kim, L. J. Miara, D. Im, Y. Wang and G. Ceder, *Nat. Mater.*, 2022, **21**, 924–931.
17 H. Fang and P. Jena, *Nat. Commun.*, 2022, **13**, 2078.
18 P. Shewmon, *Diffusion in Solids*, Springer, 2nd edn, 2016.
19 R. C. Agrawal and R. K. Gupta, *J. Mater. Sci.*, 1999, **34**, 1131–1162.
20 S. Hull, *Rep. Prog. Phys.*, 2004, **67**, 1233–1314.
21 E. Kocer, T. W. Ko and J. Behler, *Annu. Rev. Phys. Chem.*, 2022, **73**, 163–186.
22 S. Anand, M. Y. Toriyama, C. Wolverton, S. M. Haile and G. J. Snyder, *Acc. Mater. Res.*, 2022, **3**, 685–696.
23 T. Ogawa, A. Taguchi and A. Kuwabara, *npj Comput. Mater.*, 2022, **8**, 79.
24 C. Freysoldt, B. Grabowski, T. Hickel, J. Neugebauer, G. Kresse, A. Janotti and C. G. Van de Walle, *Rev. Mod. Phys.*, 2014, **86**, 253–305.
25 A. Zunger and O. I. Malyi, *Chem. Rev.*, 2021, **121**, 3031–3060.
26 H. Yildirim, A. Kinaci, M. K. Y. Chan and J. Greeley, *ACS Appl. Mater. Interfaces*, 2015, **7**, 18985–18996.
27 J. Pan, Y.-T. Cheng and Y. Qi, *Phys. Rev. B: Condens. Matter Mater. Phys.*, 2015, **91**, 134116.
28 K. Oh, D. Chang, B. Lee, D.-H. Kim, G. Yoon, I. Park, B. Kim and K. Kang, *Chem. Mater.*, 2018, **30**, 4995–5004.
29 P. Gorai, H. Long, E. Jones, S. Santhanagopalan and V. Stevanović, *J. Mater. Chem. A*, 2020, **8**, 3851–3858.
30 P. Gorai, T. Famprikis, B. Singh, V. Stevanović and P. Canepa, *Chem. Mater.*, 2021, **33**, 7484–7498.
31 B. Ruprecht, M. Wilkening, A. Feldhoff, S. Steuernagel and P. Heitjans, *Phys. Chem. Chem. Phys.*, 2009, **11**, 3071–3081.
32 A. Düvel, B. Ruprecht, P. Heitjans and M. Wilkening, *J. Phys. Chem. C*, 2011, **115**, 23784–23789.
33 A. Düvel, P. Heitjans, P. Fedorov, G. Scholz, G. Cibin, A. V. Chadwick, D. M. Pickup, S. Ramos, L. W. L. Sayle, E. K. L. Sayle, T. X. T. Sayle and D. C. Sayle, *J. Am. Chem. Soc.*, 2017, **139**, 5842–5848.
34 S. Breuer and M. Wilkening, *Dalton Trans.*, 2018, **47**, 4105–4117.
35 K. Mori, K. Sato, T. Ogawa, A. Kuwabara, S. Song, T. Saito, T. Fukunaga and T. Abe, *ACS Appl. Energy Mater.*, 2024, **7**, 7787–7797.
36 P. P. Fedorov, I. I. Buchinskaya, N. A. Ivanovskaya, V. V. Konovalova, S. V. Lavrishchev and B. P. Sobolev, *Dokl. Phys. Chem.*, 2005, **401**, 53–55.

37 K. Motohashi, T. Nakamura, Y. Kimura, Y. Uchimoto and K. Amezawa, *Solid State Ionics*, 2019, **338**, 113–120.

38 A. Düvel, *Dalton Trans.*, 2019, **48**, 859–871.

39 N. Matsui, T. Seki, K. Suzuki, M. Hirayama and R. Kanno, *ACS Appl. Energy Mater.*, 2023, **6**, 11663–11671.

40 A. Roos, F. van de Pol, R. Keim and J. Schoonman, *Solid State Ionics*, 1984, **13**, 191–203.

41 C. Rongeat, M. A. Reddy, R. Witter and M. Fichtner, *ACS Appl. Mater. Interfaces*, 2014, **6**, 2103–2110.

42 M. A. Reddy and M. Fichtner, *J. Mater. Chem.*, 2011, **21**, 17059.

43 A. Düvel, J. Bednarcik, V. Šepelák and P. Heitjan, *J. Phys. Chem. C*, 2014, **118**, 7117–7129.

44 K. Shimoda, Y. Morita, K. Noi, T. Fukunaga, Z. Ogumi and T. Abe, *ACS Energy Lett.*, 2023, **8**, 2570–2575.

45 M. V. S. Sarma and S. V. Suryanarayana, *Solid State Ionics*, 1990, **42**, 227–232.

46 M. Heise, G. Scholz, A. Düvel, P. Heitjans and E. Kemnitz, *Solid State Sci.*, 2016, **60**, 65–74.

47 M. Heise, G. Scholz, A. Düvel, P. Heitjans and E. Kemnitz, *Solid State Sci.*, 2018, **77**, 45–53.

48 S. Lunghammer, A. Düvel, P. Posch, B. Kunert, R. Resel and H. M. R. Wilkening, *Solid State Ionics*, 2019, **343**, 115067.

49 L. B. Gulina, A. F. Privalov, M. Weigler, I. V. Murin, V. Tolstoy and M. Vogel, *Appl. Magn. Reson.*, 2020, **51**, 1691–1699.

50 A. Zevgolis, B. C. Wood, Z. Mehmedović, A. T. Hall, T. C. Alves and N. Adelstein, *APL Mater.*, 2018, **6**, 047903.

51 Z. Yu, S.-L. Shang, J.-H. Seo, D. Wang, X. Luo, Q. Huang, S. Chen, J. Lu, X. Li, Z.-K. Liu and D. Wang, *Adv. Mater.*, 2017, **29**, 1605561.

52 W. Puin and P. Heitjans, *Nanostruct. Mater.*, 1995, **6**, 885–888.

53 B. Ruprecht, M. Wilkening, S. Steuernagel and P. Heitjans, *J. Mater. Chem.*, 2008, **18**, 5412–5416.

54 N. I. Sorokin, D. N. Karimov, E. A. Krivandina, Z. I. Zhmurova and O. N. Komar'kova, *Crystallogr. Rep.*, 2008, **53**, 271–277.

55 G. Kresse and J. Furthmüller, *Phys. Rev. B: Condens. Matter Mater. Phys.*, 1996, **54**, 11169–11186.

56 G. Kresse and D. Joubert, *Phys. Rev. B: Condens. Matter Mater. Phys.*, 1999, **59**, 1758–1775.

57 J. P. Perdew, A. Ruzsinszky, G. I. Csonka, O. A. Vydrov, G. E. Scuseria, L. A. Constantin, X. Zhou and K. Burke, *Phys. Rev. Lett.*, 2008, **100**, 136406.

58 A. Seko, Y. Koyama and I. Tanaka, *Phys. Rev. B: Condens. Matter Mater. Phys.*, 2009, **80**, 165122.

59 C. Freysoldt, J. Neugebauer and C. G. Van de Walle, *Phys. Rev. Lett.*, 2009, **102**, 016402.

60 Y. Kumagai and F. Oba, *Phys. Rev. B: Condens. Matter Mater. Phys.*, 2014, **89**, 195205.

61 D. Zhang, K. Yamamoto, A. Ochi, Y. Wang, T. Yoshinari, K. Nakanishi, H. Nakano, H. Miki, S. Nakanishi, H. Iba, T. Uchiyama, T. Watanabe, K. Amezawa and Y. Uchimoto, *J. Mater. Chem. A*, 2021, **9**, 406–412.

62 A. Zunger, S.-H. Wei, L. G. Ferreira and J. E. Bernard, *Phys. Rev. Lett.*, 1990, **65**, 353–356.

63 A. van de Walle, P. Tiwary, M. de Jong, D. Olmsted, M. Asta, A. Dick, D. Shin, Y. Wang, L.-Q. Chen and Z.-K. Liu, *Calphad*, 2013, **42**, 13–18.

64 G. Henkelman, B. P. Uberuaga and H. Jónsson, *J. Chem. Phys.*, 2000, **113**, 9901–9904.

65 R. Nelson, C. Ertural, J. George, V. L. Deringer, G. Hautier and R. Dronskowski, *J. Comput. Chem.*, 2020, **41**, 1931–1940.

66 R. Jinnouchi, J. Lahnsteiner, F. Karsai, G. Kresse and M. Bokdam, *Phys. Rev. Lett.*, 2019, **122**, 225701.

67 M. P. Allen and D. J. Tildesley, *Computer Simulation of Liquids*, Oxford University Press., 2nd edn, 2017.

68 S. Nosé, *J. Phys. Soc. Jpn.*, 2001, **70**, 75–77.

69 U. Matsumoto, T. Ogawa, C. A. J. Fisher, S. Kitaoka and I. Tanaka, *J. Phys. Chem. C*, 2021, **125**, 20460–20467.

70 K. Momma and F. Izumi, *J. Appl. Crystallogr.*, 2011, **44**, 1272–1276.

71 T. A. Lee, C. R. Stanek, K. J. McClellan, J. N. Mitchell and A. Navrotsky, *J. Mater. Res.*, 2008, **23**, 1105–1112.

72 M. Yoshimura, E. Tani and S. Sōmiya, *Solid State Ionics*, 1981, **3–4**, 447–481.

73 L. C. Shuller-Nickles, R. C. Ewing and U. Becker, *J. Solid State Chem.*, 2013, **197**, 550–559.

74 D. T. Thieu, M. H. Fawey, H. Bhatia, T. Diemant, V. S. K. Chakravadhanula, R. J. Behm, C. Kübel and M. Fichtner, *Adv. Funct. Mater.*, 2017, **27**, 1701051.

75 H. Nakano, T. Matsunaga, T. Mori, K. Nakanishi, Y. Morita, K. Ide, K. Okazaki, Y. Orikasa, T. Minato, K. Yamamoto, Z. Ogumi and Y. Uchimoto, *Chem. Mater.*, 2021, **33**, 459–466.

76 R. D. Shannon and C. T. Prewitt, *Acta Crystallogr.*, 1970, **B26**, 1046–1048.

77 W. Kob, *J. Phys.: Condens. Matter*, 1999, **11**, R85.

78 Y. Li and H. Ni, *Comput. Phys. Commun.*, 2023, **284**, 108599.

79 G. Krenzer, J. Klarbring, K. Tolborg, H. Rossignol, A. R. McCluskey, B. J. Morgan and A. Walsh, *Chem. Mater.*, 2023, **35**, 6133–6140.

80 R. A. De Souza, M. J. Pietrowski, U. Anselmi-Tamburini, S. Kim, Z. A. Munir and M. Martin, *Phys. Chem. Chem. Phys.*, 2008, **10**, 2067–2072.

81 B. M. Voronin and S. V. Volkov, *J. Phys. Chem. Solids*, 2001, **62**, 1349–1358.

82 E. Barsis and A. Taylor, *J. Chem. Phys.*, 1968, **48**, 4362–4367.

83 W. Bollmann and H. Henniger, *Phys. Status Solidi A*, 1972, **11**, 367–371.

84 E. Barsis and A. Taylor, *J. Chem. Phys.*, 1966, **45**, 1154–1162.

85 G. Trinquier and R. Hoffmann, *J. Phys. Chem.*, 1984, **88**, 6696–6711.

86 A. Walsh and G. W. Watson, *J. Solid State Chem.*, 2005, **178**, 1422–1428.

87 G. Laurita and R. Seshadri, *Acc. Chem. Res.*, 2022, **55**, 1004–1014.

88 N. Matsui, M. Murakami, K. Mori, T. Saito, K. Shimizu, K. Suzuki and R. Kanno, *J. Mater. Chem. A*, 2024, **12**, 3989.

89 M. G. Goesten and R. Hoffmann, *J. Am. Chem. Soc.*, 2018, **140**, 12996–13010.

90 B. Mercadier, S. W. Coles, M. Duttine, C. Legein, M. Body, O. J. Borkiewicz, O. Lebedev, B. J. Morgan, C. Masquelier and D. Dambournet, *J. Am. Chem. Soc.*, 2023, **145**, 23739–23754.